Chapter 6

Diffuse Wave-Based Smart Damage Analysis

6.1. Introduction

This chapter aims to present a damage assessment methodology based on diffuse wave analysis. The chapter includes the sections on the diffuse zone selection process followed by damage analysis. Initially, damage analysis is carried out using two pre-existing energy-based techniques. A new wavelet-based technique is proposed and compared with the existing energy-based technique. A comparative study is also carried using wavelet integrated neural network analysis and wavelet-based energy methods. A cantilever beam structure is used for testing the diffuse wave technique.

6.2. Diffuse zone selection using discrete wavelet transform

Various researchers have used a diffuse zone for qualitative and quantitative analysis of damage assessment in structural problems. The identification of diffuse field zone is a difficult process. Generalizing the concept of diffuse zone generation by considering all boundaries of structures to be reflectors is not true. But the field thus generated may be considered partially diffuse. As described by Evans and Cawley, "A diffuse field cannot strictly be generated in an enclosure if all the boundaries are specular reflectors, but in certain cases, the fields generated are approximately diffuse. If the source is non-directional (small with respect to the wavelength) and excites waves over a finite bandwidth (rather than a single frequency), all normal modes (or structural modes) of the enclosure which have natural frequencies within the excitation bandwidth can be excited simultaneously.” A single normal mode can not generate a diffuse field. The magnitude of mode distribution is not random because of the occurrence of nodes and anti-nodes. If more than one mode is excited over a finite frequency region, the movement of modes at any instance of time within the field gets superimpose. All motion patterns became uniform on increasing the modes. This stage can be approximated as a diffuse field [75].

For the selection of the diffuse zone, testing of two samples is carried out for three different impulse excitations. Two samples used in studying the diffuse zone selection include a sample with free boundary condition (FBC) and another sample with a constrained boundary condition (CBC). The purpose of selecting these two samples is that the diffuse zone will exist only in open boundary as the reflection of the waves will be absorbed in case of the constrained boundary. Starting from 2 MHz with 0.5 MHz increment for two times, a signal of 0.5-millisecond duration is used as input in this experiment for excitation of waves. Longitudinal polarized PZT transducers were used for wave generation and signal receivers. The input signal is controlled by using a function generator. The output of the diffuse signal is stored in a digital oscilloscope. All waveforms are recorded for 1000 microseconds for a total of 11000 data points. For applying dyadic scaling and shifting based on Nyquist criteria, 10080 data points are considered under analysis. After the generation of the signal, a multilevel decomposition using a discrete wavelet transform is performed for both types of the sample at all three excitation levels. Wavelet transformation using db4 is performed for five decomposition levels. The reason for selecting five levels of decomposition is to obtain a data set to study the variation that occurs in the diffuse zone. After the decomposition, 315 data of both approximate and detailed coefficients are obtained. Approximate coefficients are considered for the comparative study of samples with open and constrained boundary conditions. The results of the samples for the first excitation are shown in fig. 6.1.

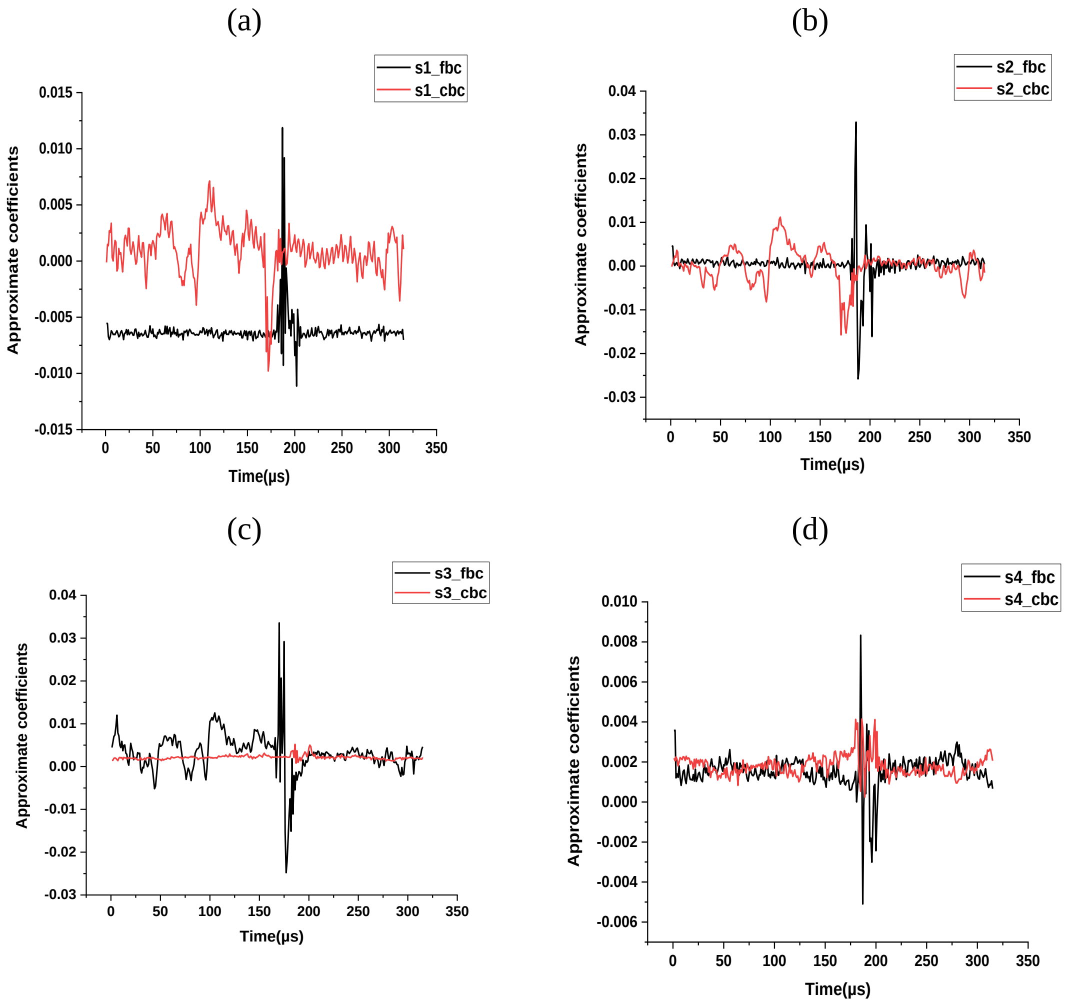
(a) (b) (c) (d)

Fig. 6.1. Comparative plots of approximate coefficients of open and constrained boundary conditions at 2MHz (a) Sensor 1; (b) Sensor 2; (c) Sensor 3; (d) Sensor 4.

The results of the second excitation for all four sensors are shown in fig. 6.2. In this figure, a spike is observed in the region between 160 and 200 microseconds.

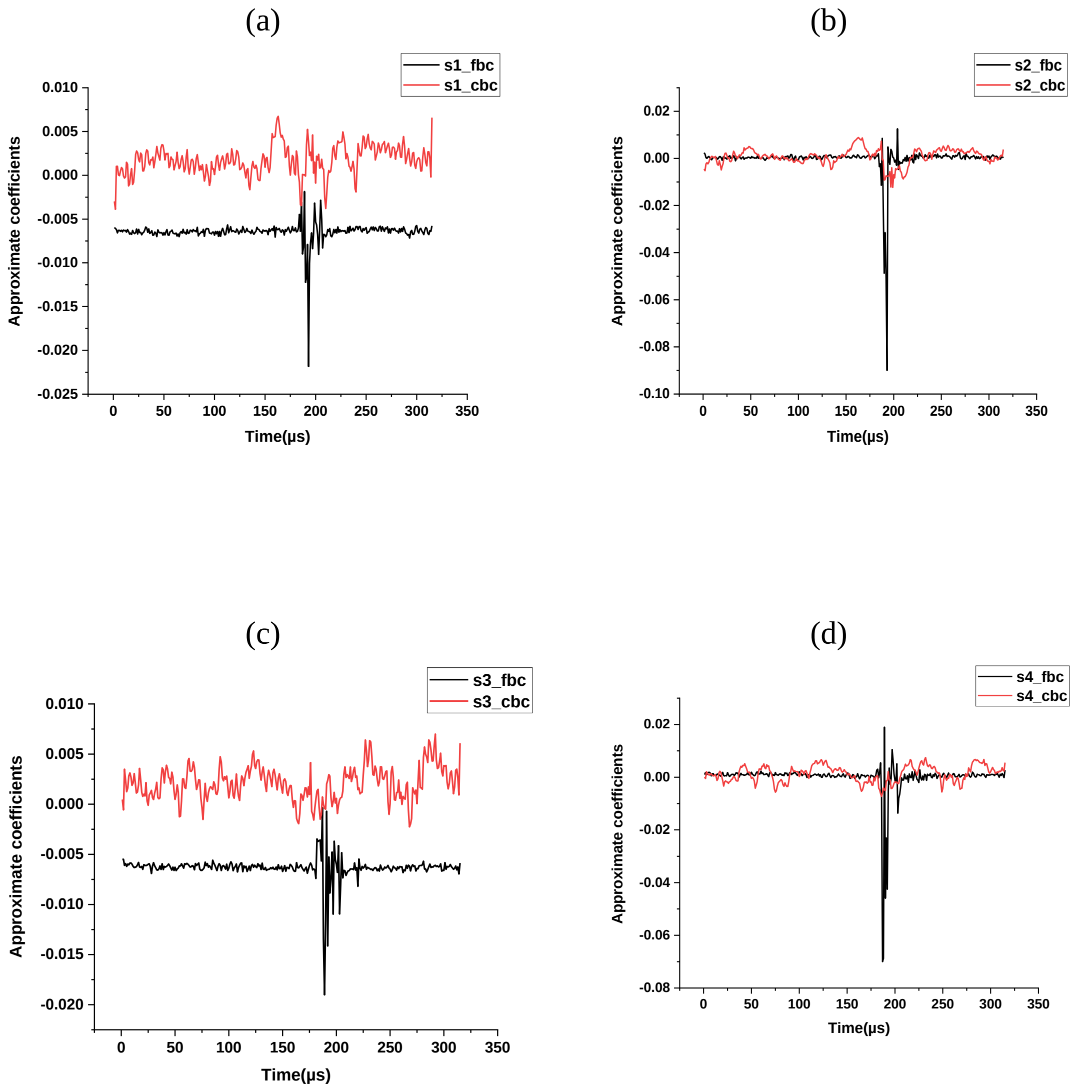

Fig. 6.2 Comparative plots of approximate coefficients of open and constrained boundary conditions at 2.5MHz (a) Sensor 1; (b) Sensor 2; (c) Sensor 3; (d) Sensor 4.

A similar signature of approximate coefficients is obtained at excitation three. Plots of four sensors are shown in fig. 6.3.

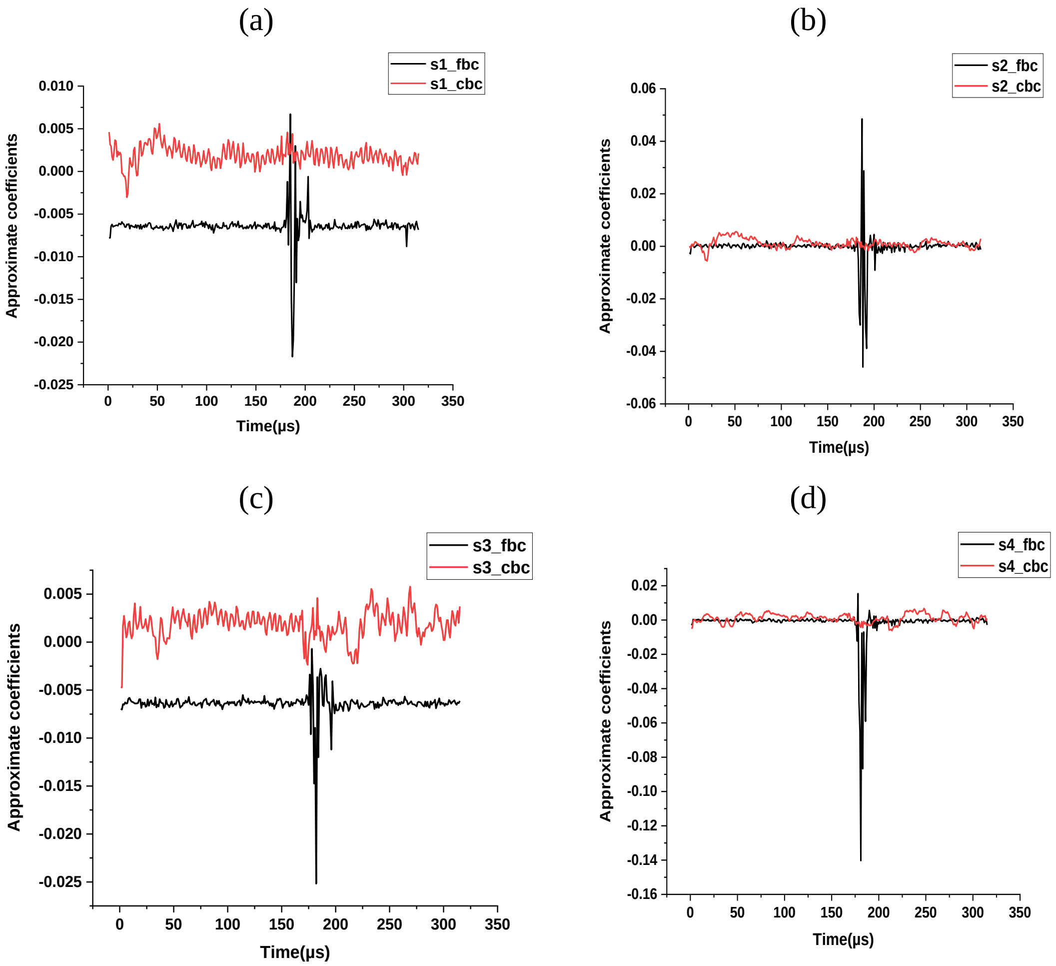

Fig. 6.3 Comparative plots of approximate coefficients of open and constrained boundary conditions at 3MHz (a) Sensor 1; (b) Sensor 2;(c) Sensor 3;(d) Sensor 4.

It is observed that samples with constrained boundaries show a comparatively smooth curve with respect to samples with open boundary conditions. In open boundary conditions, significant abrupt variation occurs in the range of time zone of 150 μs to 250 μs. It can also be related to a period when no stationary wave exists. Basics of the above logic are that reflected waves will get absorbed in the case of samples with a constrained boundary, but the same will not be the case with open boundary samples.

The analysis is repeated for the other two excitations at four different locations are shown in fig. 6.2, and fig. 6.3. Similar observations prove that the discrete wavelet transform can be useful in the detection of the diffuse zone.

6.3. Diffuse zone-based damage analysis integrated with neural network

6.3.1. Neural Network Methodology

The neural network (ANN) is a well-defined set of input, hidden, and output layers. The intelligence-based processing structure is based on the layers, which are the stimulation of neurons. Neuron transfers a weighted function from one layer to another, which gets updated based on the error value. Bias values are used with weight values for training and testing.

6.3.2. Training and testing of the model

Three phases are required for proposing an ANN architecture, which includes training, validation, and testing phases. Approximate and detail coefficients are taken as input parameters with 315 data per sample set for the ANN model. The holdout cross-validation method is used for validating the ANN data arrangement for test, train, and validation. A Tansig transfer function is used in hidden layers. Data set are created as 315 data for four different sample types. Out of the total of 1260 data, 5% data is used for validation, 10% data is used for testing, and the remaining 85% data is used for training. The bayesian regularization algorithm is used for the test, train, and validation. Network analysis is done for three different excitations.

The objective of mean square value (eq. 5.4, chapter 5) is to devise the criteria that estimate the number of hidden neurons as a function of input neurons to develop a model for damage prediction.

The error values are obtained by varying the number of neurons in the hidden layers of the neural network model using Bayesian regularization algorithm. Regression value is used in this study to evaluate the performance of the artificial neural system. The regression value is estimated using equation 5.8. The objective of the above least square estimation and regression analysis is to develop a model for damage analysis using wavelet parameters of the diffuse wave. The schematic of the developed neural network model is shown in fig. 6.4.

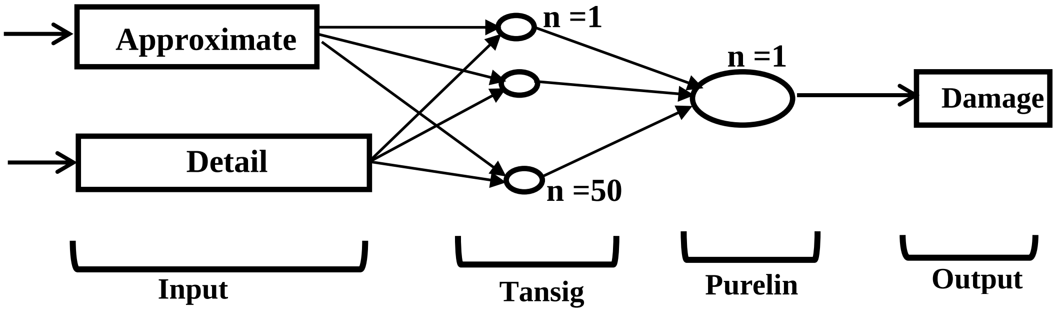

Fig. 6.4.Schematic of neural network architecture

6.3.3. Results and Discussion

Samples of different damage levels are tested for analyzing the severity of fault variations. In present work, the cantilever beam structure is used as a host material for damage analysis. A set of four sensors are mounted on the surface of each sample to obtain the change in signals at different excitations. The impulse signal is applied using a PZT transducer connected to a function generator with rectangular signal input. Signal variation is applied to obtain the different excitation levels, as defined in section 6.2 earlier. The output of the signal is stored in a digital oscilloscope for further analysis. Further discrete wavelet transform is applied on these output signals to obtain approximate and detail coefficients parameters, which are used as input data for the designed neural network. Damage volumetric ratio values obtained using equation 4.6 is set as target values in the neural network perceptron model. The hold out analysis provides a logical selection of test and train data set. Moreover, the hold out analysis also eliminates the possibility of overfitting and underfitting conditions. The Bayesian regularization back-propagation algorithm is used in this study for designing the neural network. Testing and training regression values are above the acceptable limit of 90%. Epoch is set to a maximum limit of 1000.

Fig. 6.5 show the performance plot of the multilayer perceptron model, based on the mean square error of the developed model. The graph proves the successful working of the developed model with high confidence and the least error values. Mean square error plots of different data set at various loading show that the model predicts very well the target values. Table 6.1 presents the obtained values of different ANN parameters used in the analysis. Regression values are analyzed for the acceptability of the developed ANN model. From the table, it is clear that all regression values are above the R = 0.90 value. Values of data comparison by regression analysis prove that the developed ANN model works well within the acceptable range of regression and standard error.

Table 6.1. Performance effectiveness of neural network model at different loads

Level	Load	Training (R-value)	Testing (R-value)	All (R-value)	Epoch	Best training performance
2MHz	Sensor 1	0.99349	0.99166	0.99315	188	7.1442e^{-06}
	Sensor 2	0.98436	0.96385	0.98176	45	5.8428e^{-06}
	Sensor 3	0.99828	0.99548	0.99773	149	5.4669e^{-06}
	Sensor 4	0.90612	0.97213	0.96071	11	5.7171e^{-06}
2.5MHz	Sensor 1	0.93753	0.92414	0.92631	83	5.7345e^{-06}
	Sensor 2	0.91834	0.93682	0.91704	166	5.3065e^{-06}
	Sensor 3	0.93712	0.94723	0.94902	106	6.0059e^{-06}
	Sensor 4	0.99835	0.99619	0.98031	34	6.1915e^{-06}
3MHz	Sensor 1	0.94821	0.95023	0.93276	22	6.4511e^{-06}
	Sensor 2	0.92784	0.93207	0.94026	107	4.1733e^{-06}
	Sensor 3	0.98398	0.99662	0.99792	24	7.0578e^{-06}
	Sensor 4	0.96241	0.95802	0.94803	149	7.1658e^{-06}

Mean square error for test and train data reduces and became constant after 40 epoch values, as shown in fig. 6.5. Fig. 6.5(a) shows that mean square error reduces initially for 2 MHz. But a steep reduction is observed near 50 epochs. A constant value is attained after 60 epoch value. In fig 6.5(b)**,** the test and train curve separates near 35 epochs but became constant after 40 epoch value. Fig. 6.5(c) shows a constant reduction in mean square error curve, which became constant at 80 epochs. Fig. 6.5(d) shows a steep reduction in mean square error near four epochs, and the curve became constant after 11 epoch value where the maximum gradient is reached.

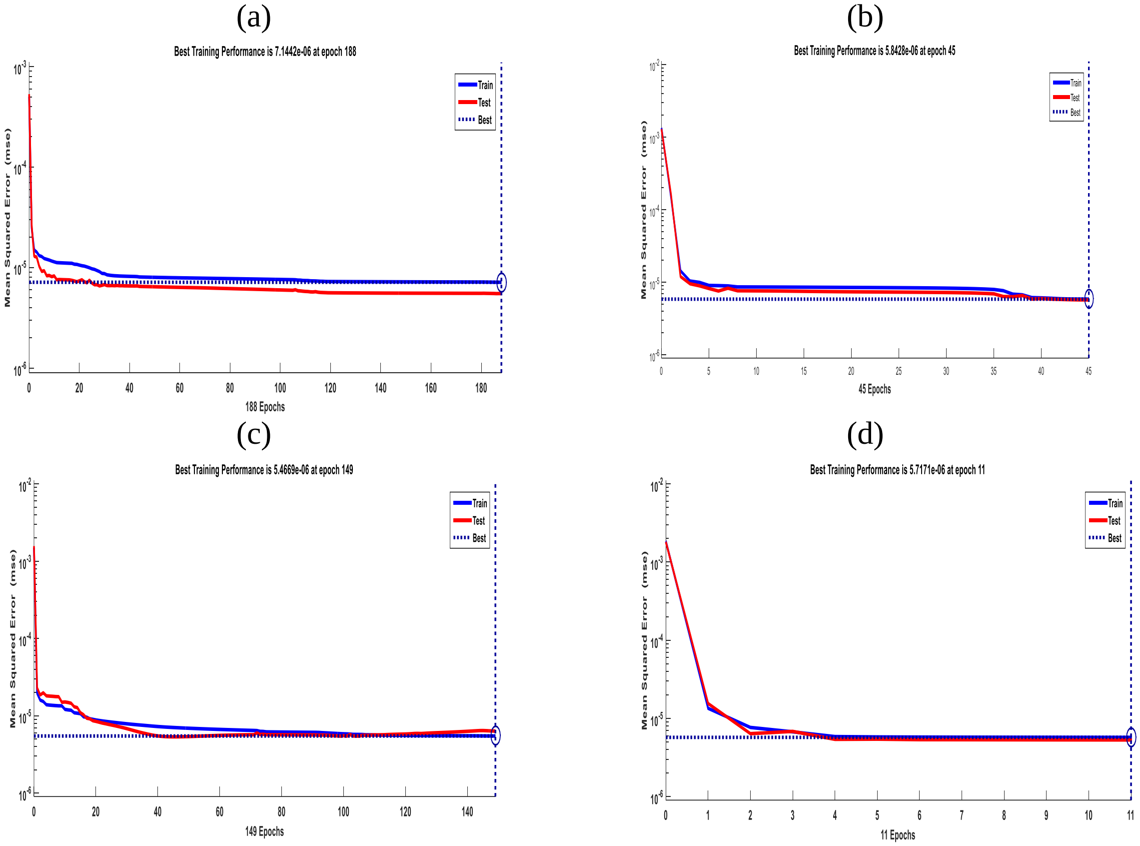

Fig. 6.5. Mean square error plots of different sensor @ 2MHz: (a) Sensor 1; (b) Sensor 2; (c) Sensor 3; (d) Sensor 4.

For 2.5 MHz, mean square error reduces initially, as presented in fig 6.6(a). A considerable decline in error value is observed near 40 epochs and became constant after 50 epoch. Similarly, in fig 6.6(b), test and train curves are separated near 60 epochs but became close after 120 epoch value. In sensor 3, a constant reduction in mean square error curve is obtained, which became constant at 50 epochs, as shown in fig. 6.6(c). Fig. 6.6(d) shows a steep reduction in mean square error near eight epochs, and the curve became constant after 10 epoch value.

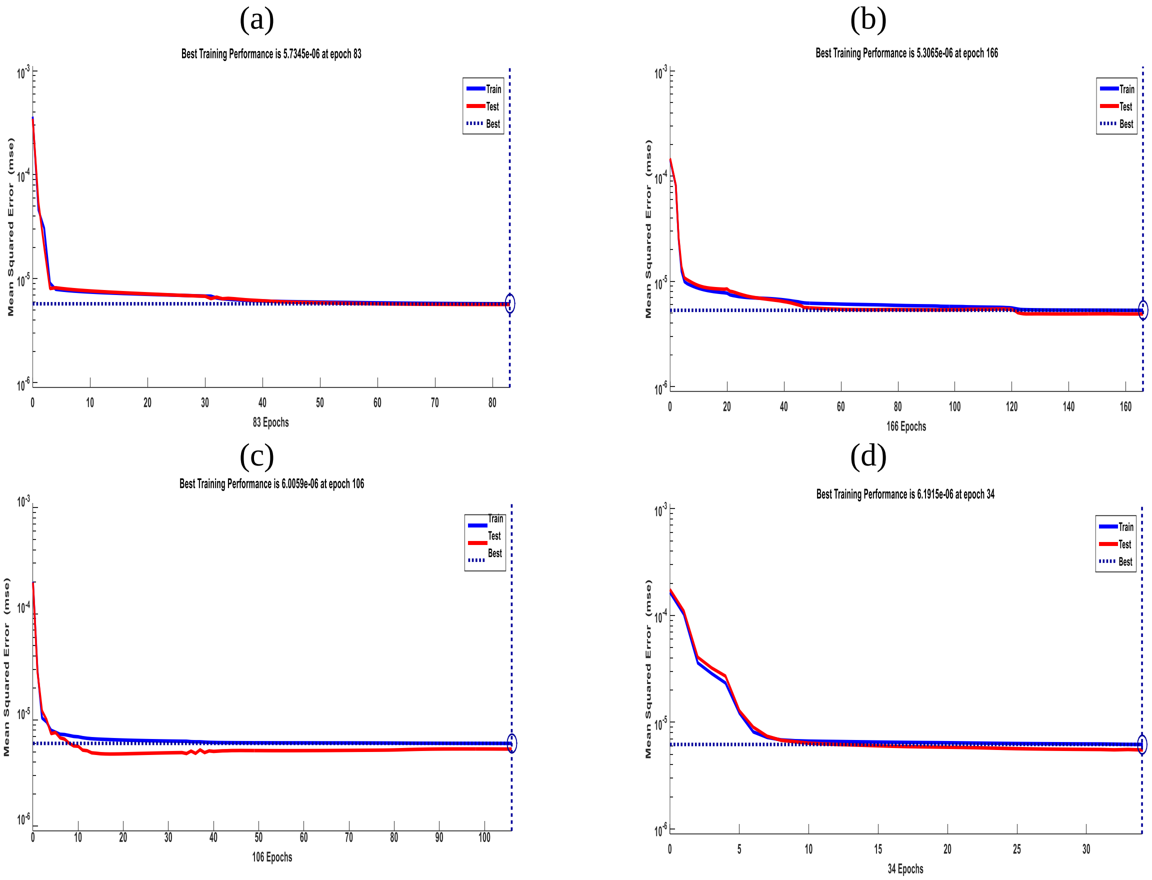

Fig. 6.6. Mean square error plots of different sensor at 2MHz: (a) Sensor 1; (b) Sensor 2; (c) Sensor 3; (d) Sensor 4.

As shown in fig 6.7(a), mean square error reduces initially for 3 MHz. Reduction in error value is observed near six epochs and became constant after eight epoch. Similarly, in fig 6.7(b), test and train curve are separated near 70 epochs but became close after 800 epoch value. In fig 6.7(c), random reduction in mean square error curve is obtained, which became constant at 20 epoch. Fig. 6.7(d) shows a steep reduction in mean square error until 50 epochs, and the curve became constant after 100 epoch value.

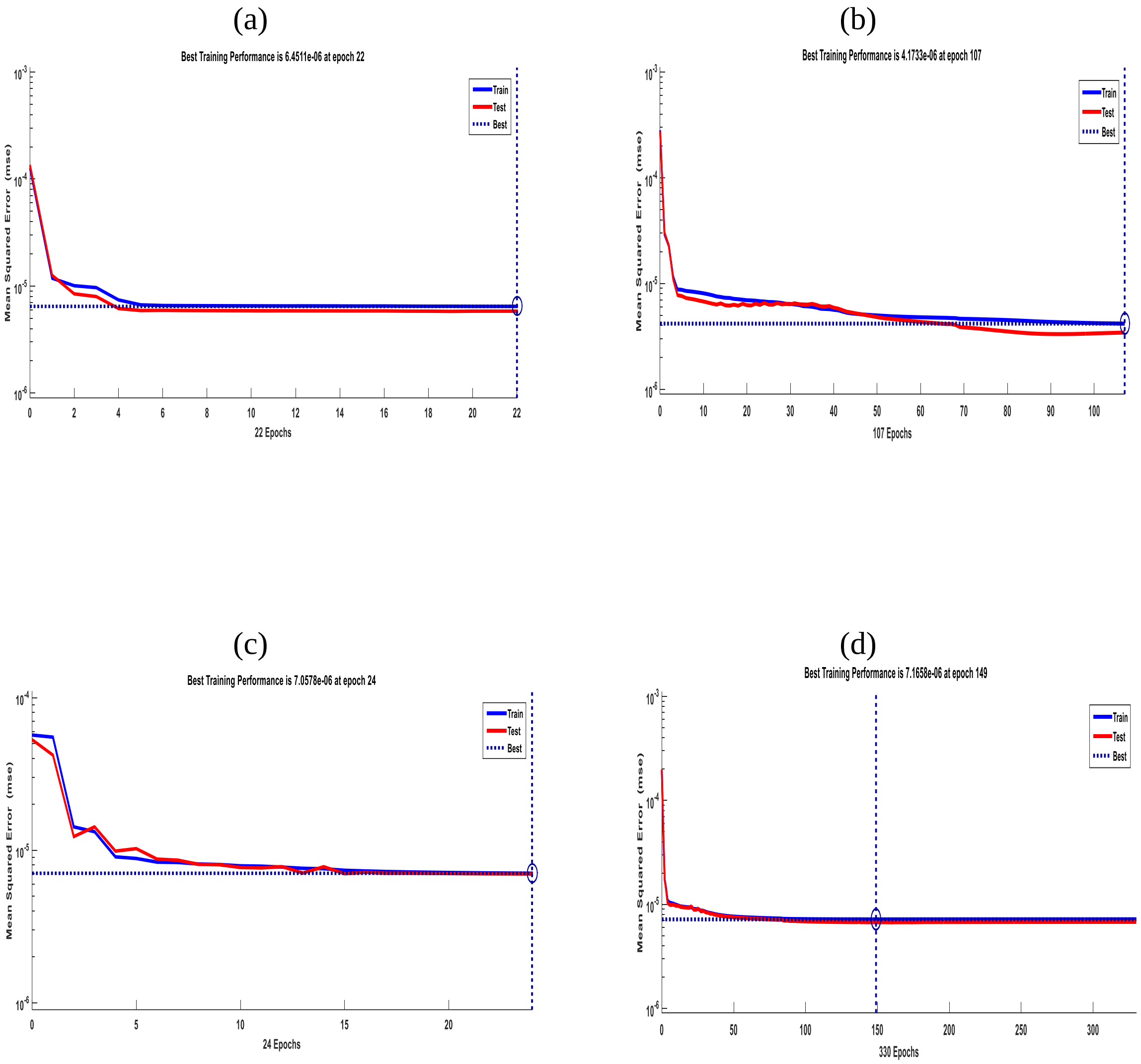
(a)
(b)
(c)
(d)

Fig. 6.7. Mean square error plots of different sensor at 2MHz: (a) Sensor 1; (b) Sensor 2; (c) Sensor 3; (d) Sensor 4.

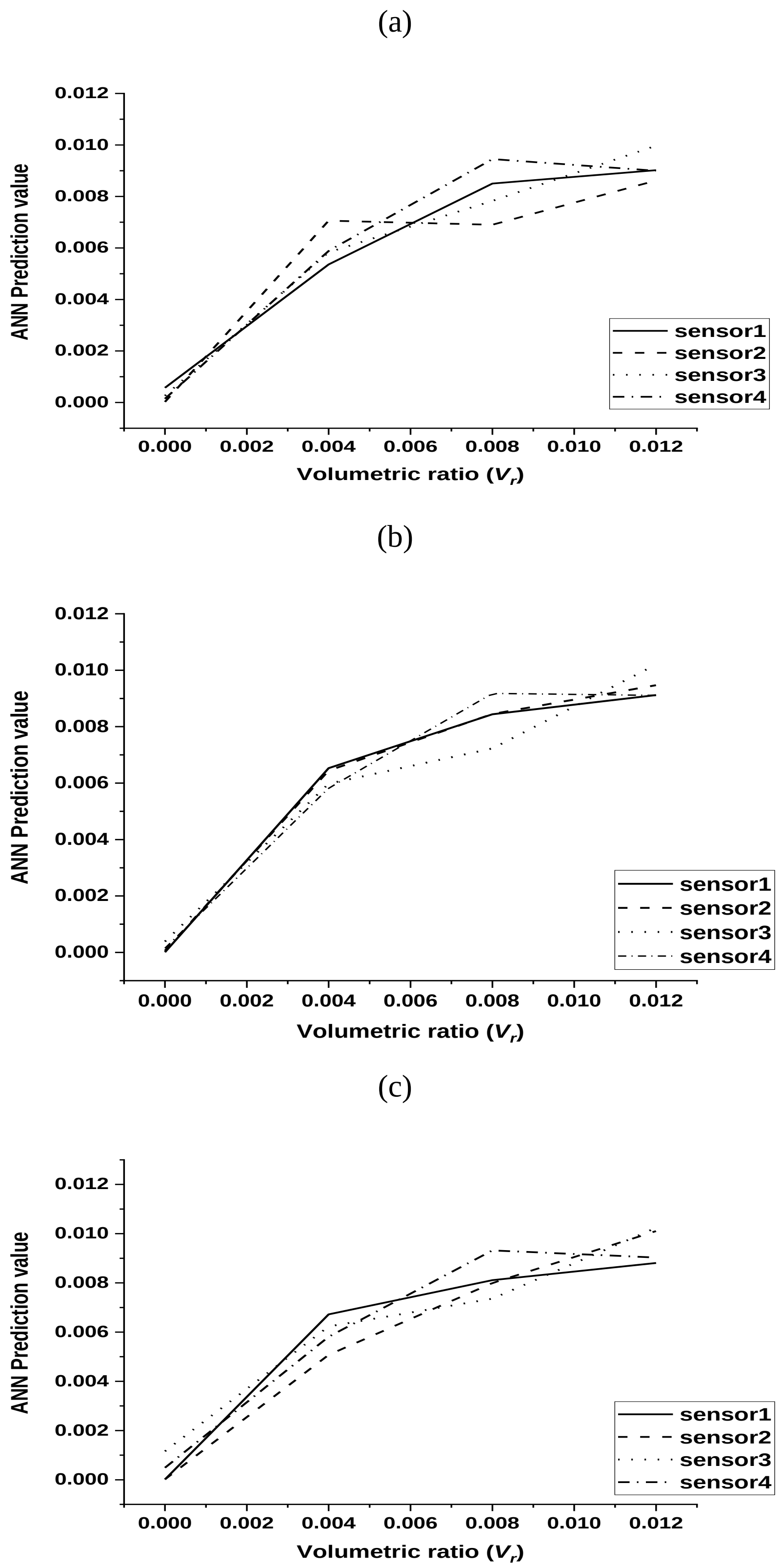

Fig. 6.8. Comparison of ANN-based output to the target values at different excitation levels: (a) 2MHz, (b) 2.5MHz, (c) 3MHz

Fig. 6.8 shows a comparison of the volumetric damage ratio for various sensors at different excitation levels. Variations in damage prediction by developed neural network model with volumetric damage ratio for different sensors are shown. It is observed that in all three excitation levels, the trend of variation is similar and well within the acceptable range. The following conclusions can be drawn based on the damage prediction:

1) Over and under prediction of target values are observed using the ANN approach. Random variation may be due to the presence of noise in the signal.
2) A good agreement in neural network prediction and target value occurs. The advantage of using this model is that it eliminates the effect of noise present in the signal.

6.4. Wavelet-based residual energy method using a diffuse zone

For the quantitative assessment of damage, three methods for three excitations are considered. Methods used in the research include time-domain differencing, Spectrogram differencing, and wavelet-based residual energy. The strategy applied in all three methods is computing residual energy parameters of the difference between two signals. These signals involve the parameters of healthy and damaged samples.

6.4.1. Time domain differencing (Conventional concept)

The simplest way for the comparison of signals is by subtracting one signal from another. Considering a reference signal $S_r(t)$ and measured signal $S_m(t)$ in time domain frame for a fixed time length T. Let sampling frequency be denoted as f_s and sampled signal as $S_r(n)$ and $S_m(n)$ respectively. Here n corresponds to sample at time $\frac{n}{f_s}$, having length$N = f_s * T$. The basic criteria of comparing two signals in the time domain frame are simple subtraction.

$$\Delta(n) = S_m(n) - S_r(n) \tag{6.1}$$

For $\Delta(n)$ to be an independent parameter from the amplitude of the original signal scaling of measured and reference signal is performed as follows**:**

$$\widetilde{S_m}(n) = \frac{S_m(n)}{\sqrt{\sum_{n=0}^{N-1} S_m^2(n)}} \tag{6.2}$$

$$\beta = \frac{\sum_{n=0}^{N-1} \widetilde{S_m}(n)\ S_r(n)}{\sum_{n=0}^{N-1} S_r^2(n)} \tag{6.3}$$

$$\tilde{\Delta}(n) = \widetilde{S_m}(n) - \beta * S_r(n) \tag{6.4}$$

The measured signal is normalized with the help of weight function β. The function β of the reference signal is calculated, such that it minimizes the mean square error between $\widetilde{S_m}(n)$(unity energy measured signal) and scaled reference signal. Parameter $\Delta(n)$ is considered as an amplitude-dependent measurement of signal difference. The energy of $\tilde{\Delta}(n)$ within a specific time window is considered as temporal residual energy which is calculated as follows:

$$Etd = \sum_{n=n_1}^{n_2} \tilde{\Delta}^2 (n) \tag{6.5}$$

Symbols n_1 and n_2 signify the initial and final indices related to the time window under consideration.

6.4.2. Spectrogram differencing (Conventional concept)

Time-frequency analysis for non-stationary diffuse signals provides an acceptable process for comparison of two signals. Let short-time Fourier transform (STFT) for spectrogram computation of a signal $S(n)$ of length N is defined as:

$$Z(n,k) = \sum_{m=0}^{N-1} S(m)\omega(m-n)e^{-i2\pi km/M} \tag{6.6}$$

Where $\omega(n)$ is window function of length $\mathrm{M} < N$, and the frequency index k $(0 \leq k < M)$ is related to frequency as follows:

$$f = \frac{k}{M} f_s \tag{6.7}$$

Initially, a signal $Z(n,k)$ is not computed for the individual value of n, but a resampling factor X is specified. Thus $Z(n,k)$ is obtained for each nX^{th} value of where $n = 0, 1, 2, \ldots$

$$Z(n,k) = \sum_{m=0}^{N-1} S(m)\omega(m - nX)e^{-i2\pi km/M} \tag{6.8}$$

As n is now related to continuous-time *(t)* by:

$$t = \frac{nX}{f_s} \tag{6.9}$$

Modulus value of complex STFT $|Z(n,k)|$is considered as spectrogram. Spectrogram differencing, similar to time domain differencing, is carried out considering reference signal, $Z_r(n,k)$, and measured signal $Z_m(n,k)$. The normalization process is applied before subtracting the reference signal from the measured signal. In normalization, both spectrograms are normalized globally to unity energy. The process is carried out within the window of interest before differencing. The difference between two spectrogram $\delta(n,k)$ is formulated as follows:

$$\delta(n,k) = \frac{|Z_m(n,k)|}{\sqrt{\sum_{\tilde{n}=n_1}^{n_2} \sum_{\tilde{k}=k_1}^{k_2} Z_m(\tilde{n},\tilde{k}) Z_m^*(\tilde{n},\tilde{k})}} - \frac{|Z_r(n,k)|}{\sqrt{\sum_{\tilde{n}=n_1}^{n_2} \sum_{\tilde{k}=k_1}^{k_2} Z_r(\tilde{n},\tilde{k}) Z_r^*(\tilde{n},\tilde{k})}} \tag{6.10}$$

The difference in energy using the above methodology is considered as spectral residual energy, defined as follows:

$$ESpgD = \sum_{n=n_1}^{n_2} \sum_{k=k_1}^{k_2} \delta^2(n,k) \qquad (6.11)$$

6.4.3. Wavelet-based residual energy method (Developed concept)

Signal processing is a crucial issue to extract information from the received signal to decide whether some damage has developed in the structure. As compared to guided wave-based methods, signal processing for diffuse ultrasonic waves for SHM is very difficult due to the complex nature of the energy distribution. While Fourier analysis does not provide information about what frequency appears at what instant of time, the wavelet-based analysis yields an image of time-frequency pattern so, it is preferred for non-stationary signals. Data cleansing is often required to remove the noise, which generally sensor receives from various sources. Discrete wavelet denoising using Daubechies wavelet is often used to remove local high-frequency noise. A wavelet transform can be expressed as

$$u \approx \sum_i u_i^j \varphi_i^j + \sum_i d_i^j \psi_i^j \qquad (6.12)$$

Where φ_i^j and ψ_i^j are called as scaling function and wavelet, respectively. The process of wavelet transform simplifies when we use refinement relations. The basis function at a lower level j can be expressed in terms of the basic functions of higher level $j+1$ as

$$\varphi_k^j = \sum_i h_i \varphi_i^{j+1} \tag{6.13}$$

and

$$\psi_k^j = \sum_i g_i \varphi_i^{j+1} \tag{6.14}$$

The coefficients h_i and g_i are known as low and high pass filter coefficients. These filter coefficients split a signal into high and low-frequency signals. It can be expressed as

$$u \approx \sum_i u_i^0 \varphi_i^0 + \sum_{j=0}^{n} \sum_i d_i^j \psi_i^j \tag{6.15}$$

Wavelet transform is used for all signals (healthy and defective plates). Generally high-frequency signal contains noise, so we eliminated the highest level frequency part of the signal, and the signal is reconstructed, which is represented here as u_i^j. The remaining signal is normalized to unity energy as

$$x_i = \frac{u_i^j}{\sqrt{\sum_i \left(u_i^j\right)^2}} \tag{6.16}$$

Similar to spectral residual energy mentioned in section 6.4.2, where a short-time Fourier transform is used, we used wavelet and calculated residual energy, which can be called wavelet-based residual energy ($WBRE$). It is calculated as:

$$U_i^0 = \frac{u_i^0}{\sqrt{\sum_i \left(u_i^0\right)^2 + \sum_j \sum_i \left(d_i^j\right)^2}} \tag{6.17a}$$

$$D_i^j = \frac{d_i^j}{\sqrt{\sum_i \left(u_i^0\right)^2 + \sum_j \sum_i \left(d_i^j\right)^2}} \tag{6.17b}$$

$$E_{HP} = \sum_i (U_i^0)_{HP}^2 + \sum_j \sum_i \left(D_i^j\right)_{HP}^2 \tag{6.17c}$$

$$Wbre = E_{HP} - E_{DP} \tag{6.17d}$$

Where subscript HP and DP indicates healthy and defective plates.

6.4.4. Results and Discussion

Measurement for diffuse wave-based energy analysis is made on four different samples. Specimens with cantilever geometry are used for experimentation. As wave reflections from the boundary have a major role in obtaining diffuse wave signals, therefore samples with through notches are made as defined in chapter 5, section 5.2.2. Data obtained using the storage oscilloscope is analyzed using three techniques described in section 6.4. In the present analysis signal of a healthy sample is considered as a reference for every method. Energy-based on time-domain differencing is calculated for all the measures signals. A similar procedure is followed for the Spectrogram differencing technique and wavelet-based residual energy method. Fig. 6.9 shows the plots of residual energy using three defined techniques at the excitation frequency of 2 MHz. Signals are received at four different locations using sensors. It can be noted that residual energy in all four sensors correlates to the defect size. The time-domain differencing method shows less variation compared to the other two used methods.

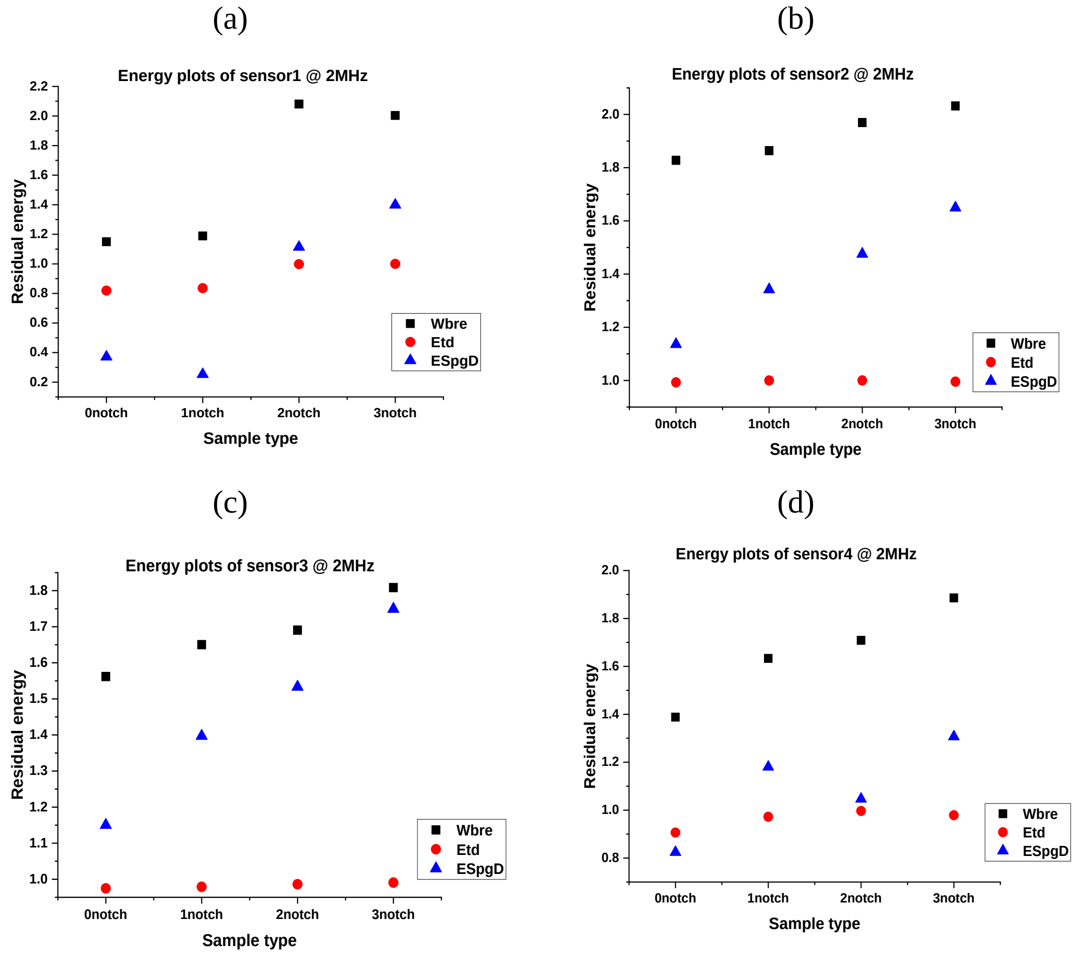

Fig. 6.9. Variation of residual energy @ 2MHz: (a) Sensor Location 1; (b) Sensor Location 2; (c) Sensor Location 3; (d) Sensor Location 4

Residual energy plots for the second level of excitation at 2.5MHz is shown in Fig. 6.10. It is clear from the figure that a good linearly approximated correlation exists for all four sensor positions.

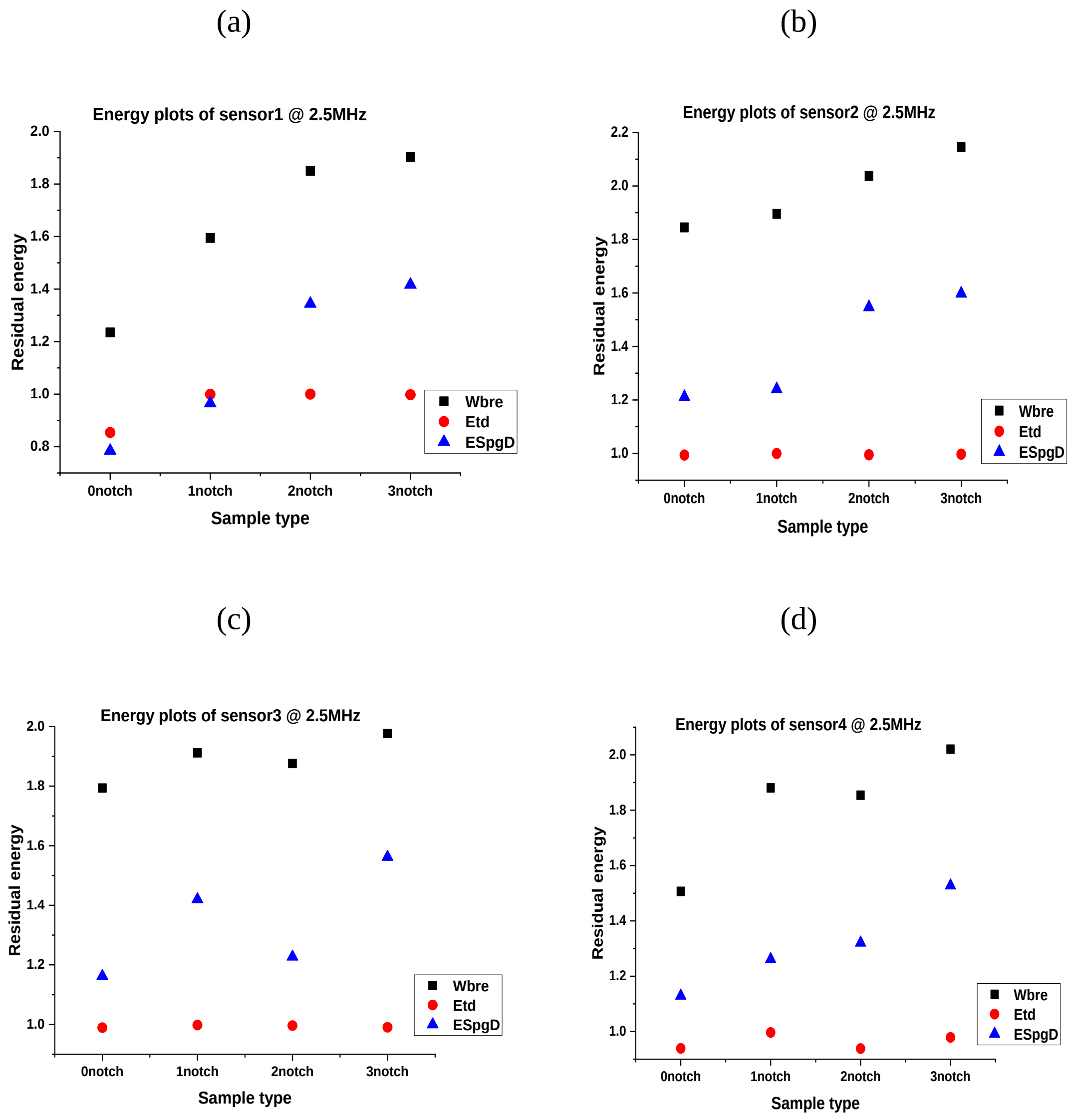
(a)

(b)

(c)

(d)

Fig. 6.10. Variation of residual energy @ 2.5MHz:(a) Sensor Location 1; (b) Sensor Location 2; (c) Sensor Location 3; (d) Sensor Location 4

Fig. 6.11 shows residual energy plots of higher excitation level at 3 MHz. At this level, a good correlation is observed for all three methods relative to all four sensor locations.

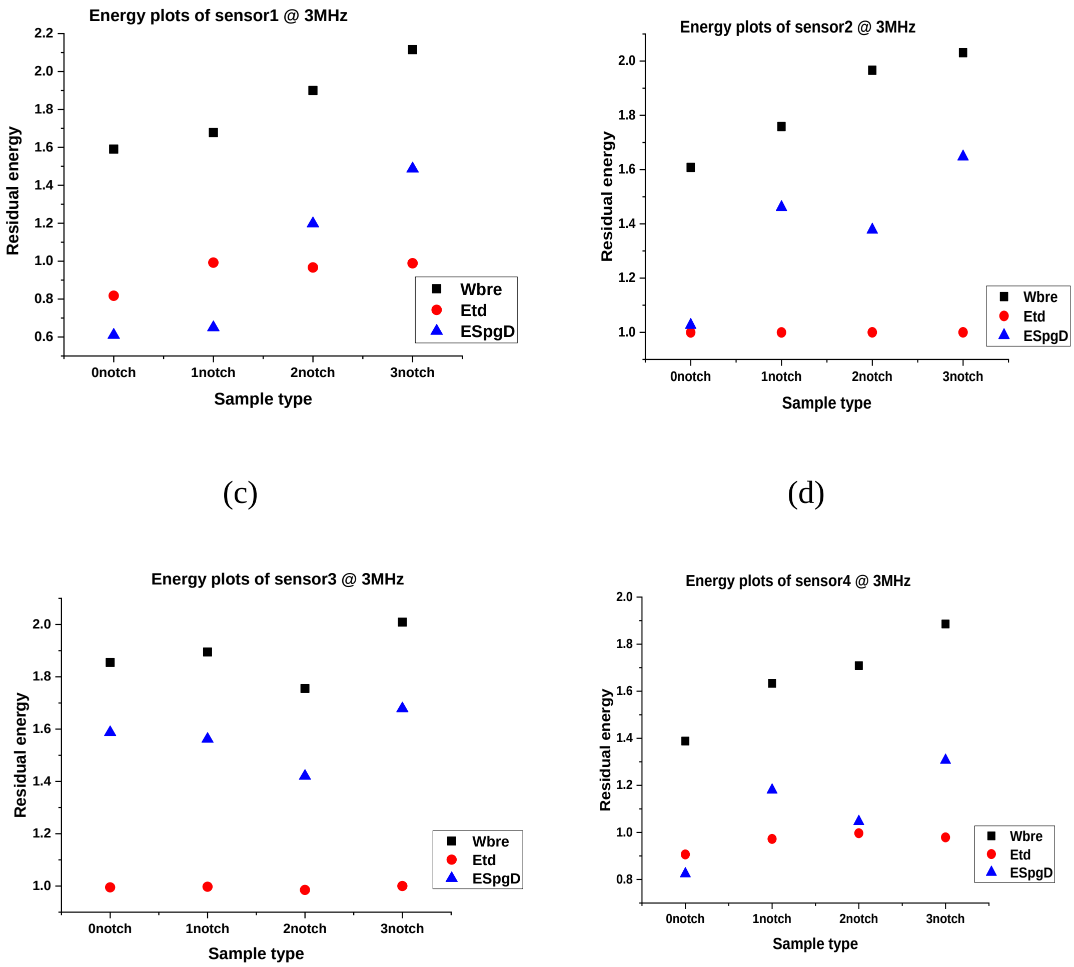

(a)

(b)

(c)

(d)

Fig. 6.11. Variation of residual energy @ 3MHz: (a) Sensor Location 1; (b) Sensor Location 2; (c) Sensor Location 3; (d) Sensor Location 4

All the plots show a common trend of increasing the residual energy with an increase in the damage size. In all the above cases, although the time-domain differencing method gave a positive response for estimating defect size, results show a low level of performance ability. Plots related to the Spectrogram differencing based residual energy method show a better capability for damage assessment compared to the time-domain differencing method. Novel development of the wavelet-based residual energy method proves high-performance ability in the detection of damage present in the structure. As compared to pre-existing techniques, the wavelet-based technique shows a strong correlation with a high degree of likelihood of damage assessment.